

Factors Influencing Computational Predictability of Aerodynamic Losses in a Turbine Nozzle Guide Vane Flow

Özhan H. Turgut¹ & Cengiz Camci²

Dept.of Aerospace Engineering, The Pennsylvania State University, University Park, PA,16802

This paper deals with the computational predictability of aerodynamic losses in a turbine nozzle guide vane (*NGV*) flow. The paper shows that 3D computations of Reynolds Averaged Navier Stokes equations have the ability to adequately represent viscous losses in the presence of laminar flows, transitional regions and fully turbulent flow areas in the *NGV* of an HP turbine stage. The Axial Flow Turbine Research Facility AFTRF used for the present experimental results has an annular nozzle guide vane assembly and a 29 bladed HP turbine rotor spinning at 1330 rpm. The *NGV* inlet and exit Reynolds numbers based on midspan axial chord are around 300,000 and 900,000, respectively. A general purpose finite-volume 3D flow solver with a SST k- ω turbulence model is employed. The current computational study benefits from these carefully executed aerodynamic experiments in the *NGV* of the AFTRF. The grid independence study is performed with static pressure coefficient distribution at the mid-span of the vane and the total pressure coefficient at the *NGV* exit. The effect of grid structure on aerodynamic loss generation is emphasized. The flow transition effect and the influence of corner fillets at the vane-endwall junction are also studied. The velocity distributions and the total pressure coefficient at the *NGV* exit plane are in very good agreement with the experimental data. This validation study shows that the effect of future geometrical modifications on the turbine endwall surfaces will be predicted reasonably accurately. The current study also indicates that an accurately defined turbine stage geometry, a properly prepared block structured/body fitted grid, a state of the art transitional flow implementation, inclusion of fillets and realistic boundary conditions coming from high resolution turbine experiments are all essential ingredients of a successful turbine *NGV* aerodynamic loss quantification via computations. This validation study forms the basis for the succesful future generation of non-axisymmetric endwall surface modifications in AFTRF research efforts.

¹ Currently, Development Specialist, Praxair Inc., Turbomachinery Aerodynamics, 175 East Park Dr., Tonawanda NY 14150.

² Professor of Aerospace Engineering, ASME Fellow, Dept. of Aerospace Eng., 223 Hammond Bldg., University Park PA 16802.

Nomenclature

c	= Midspan axial chord length of AFTRF nozzle guide vane, [m]
C_p	= Static pressure coefficient, $\frac{P_1 - P_2}{0.5 \rho U_m^2}$
C_p'	= Static pressure coefficient, $\frac{P - P_{01}}{0.5 \rho V_{x1}^2}$
C_{pt}	= Total pressure coefficient, $\frac{P_{02} - P_{01}}{0.5 \rho U_m^2}$
k	= Turbulence kinetic energy, [m^2/s^2]
P	= Static pressure, [Pa]
P_0	= Total pressure, [Pa]
$Re_{\theta t}$	= Momentum-thickness Reynolds number
T_0	= Total temperature, [K]
U_m	= Blade speed at mean radius, [m/s]
V	= Velocity magnitude, [m/s]
V_x	= Axial velocity component
V_r	= Radial velocity component
V_θ	= Circumferential velocity component
x	= Axial distance from nozzle guide vane leading edge, [m]
y^+	= Non-dimensional wall coordinate, $\frac{\sqrt{\tau_w / \rho} \cdot y_p}{\nu}$
y_p	= First grid height off the wall, [m]
γ	= Intermittency
ν	= Kinematic viscosity, [m^2/s]
ρ	= Density, [kg/s]
τ_w	= Wall shear stress [Pa]
ω	= Turbulent frequency [1/s]
1	= One axial chord upstream of nozzle guide vane leading edge
2	= Nozzle guide vane exit plane, $\frac{x}{c} = 1.025$
3	= Turbine rotor exit plane
N	= Turbine nozzle guide vane
R	= Turbine rotor blade
SST	= Shear stress transport
TKE	= Turbulence kinetic energy

I. Introduction

The viscous flow through a turbine nozzle guide vane (*NGV*) is one of the most complex internal flows that are highly three dimensional, dissipative and unsteady. The boundary layers in *NGV* flows may well contain laminar, transitional and fully turbulent flow regimes simultaneously. The high turning angle of the vanes and the momentum deficit in the inlet endwall boundary layer lead to secondary flows with significant mean kinetic energy loss. *NGV* wakes as turbulent free shear layers also play a significant role in the final level of aerodynamic losses. According to Denton [1] about one third of the total aerodynamic loss in a turbine passage is due to endwall losses. Researchers have been trying to understand the generation mechanisms of secondary flows since 1950's and trying to minimize the losses related to these flows. A comprehensive review by Sieverding [2] presents the experimental measurements on secondary flows and endwall boundary layers until 1985. Later on, Langston [3] reviewed the papers until 2001, which were related to the secondary flows, including the flow structure investigation either by experiments or by numerical methods and new approaches to reduce the secondary flow related losses. Although experiments provide valuable results in an actual turbine passage, it is still time consuming and costly to set up full scale turbine experiments under actual operating conditions at a high spatial resolution. This investigation shows that the highly three-dimensional secondary flows in a turbine *NGV* passage can be effectively quantified by computational fluid dynamics (CFD) not only for static pressure and velocity vector magnitudes but also for viscous/dissipative losses that are termed as aerodynamic losses throughout this paper. The experimental viscous flow data set and the *NGV* geometrical details used in this paper are also available in open literature from the authors of this paper. Availability of such a turbine stage geometry and associated experimental data is helpful for validating a viscous flow solvers to be implemented in any turbomachinery design system.

Three-dimensional Navier-Stokes equations based CFD using Reynolds averaging has been used as a flow prediction tool for turbine flows since 1980s. Hah [4] developed his three-dimensional compressible Navier-Stokes scheme for turbomachinery applications as early as 1984. Good agreement with measured airfoil static pressure distribution was achieved, however, mass-averaged loss coefficient was over-predicted. Moore and Moore [5] calculated turbine performance by an elliptic flow solver. Mass-averaged total pressure loss values within the passage and downstream of the blade were predicted with good agreement with the measured data. Dorney and Davis [6] analyzed aerodynamics and heat transfer for a linear turbine cascade using a three-dimensional Navier-Stokes flow solver. They presented a grid resolution study and importance of the transition modeling. They suggested that approximately 900,000 grid points for a single passage were sufficient to obtain grid independent solutions. The area-

averaged loss was calculated within 2% error margin with the finest grid. Harvey et al. [7] applied non-axisymmetric endwall contouring to both vane and blade of the Rolls-Royce Trent 500 engine intermediate pressure turbine. Their predicted efficiency improvement is closer to the measured value. Nagel and Baier [8] aimed to rise the efficiency of the turbine *NGV* by developing a combined design of both vanes and the endwall. A 3D compressible transitional Reynolds Averaged Navier-Stokes (RANS) solver was used for the flow simulation. Airfoil static pressure distribution was in good agreement with measured data. The aerodynamic loss distribution contours and the values are similar to the experimental measurements.

The users of computational fluid dynamics usually accept that that it does not provide an exact solution to the general fluid flow problem due to the mathematical nature of the governing equations. There are always inherent errors related to this numerical approach. The types of errors related to CFD simulations governed by partial differential equations (PDE) are discussed in detail by Oberkampf and Blottner [9]. Mainly four types of errors exist: i) errors related to physical modeling, ii) numerical discretization errors, iii) errors in programming, and iv) errors related to computer round-off. Physical modeling errors could arise from the mathematical expressions for viscous/inviscid flows, turbulence modeling, transitional flow representation, boundary conditions, etc. Errors in discretization of PDEs, boundary conditions and the resolution of the grid may be included in numerical discretization errors. A more recent study by Denton entitled "Some Limitations of Turbomachinery CFD" [10] discusses the types of CFD errors more specific to turbomachinery applications. The types of turbomachinery CFD errors are summarized as numerical errors, modeling errors, errors related to boundary conditions, and the geometrical considerations of the blade, seal and tip clearances, etc. It is suggested by Denton that CFD is to be used as a comparison tool, instead of a performance prediction method. It is also noted that CFD should be calibrated based on experiments, not the vice versa.

Keeping in mind the limitations and the errors in CFD prediction, this paper aims to simulate the fluid flow through a turbine *NGV*. The experimental facility used in the generation of the experimental data sets are described. The current *NGV* experiments reported in this paper are all obtained in a single stage HP turbine flow simulator including a 29 bladed rotor section. A comprehensive study are presented with both unstructured and block-structured body fitted structured meshes. The necessity for high grid resolution near wall boundaries are discussed. The fluid flow in a turbine *NGV* is likely to be transitional especially near the suction side of the vanes, as long as the vanes are not film cooled. Fully turbulent and transitional flow calculations are compared and the influence of corner fillets at the vane-endwall junction are emphasized. The computed *NGV* exit flow conditions are compared to the available experimental data set

previously obtained in Axial Flow Turbine Research Facility (AFTRF), [11] of Turbomachinery Aero-Heat Transfer Laboratory.

Present investigation showed that the current computational approach was successful in simulating steady viscous flows of our turbine experiments performed in the large scale, low speed rotating turbine stage AFTRF operated under full Re number simulation conditions. The non-dimensional aerodynamic loading distributions on rotating blades were also well simulated. The aerodynamic losses in the *NGV* passage of the current HP stage were successfully obtained from the computational simulations. The *NGV* wake, secondary flow structure and hub endwall boundary layer were all effectively simulated. The general simulation approach developed in this paper forms a useful foundation for the development of new *NGV* aerodynamic loss reduction features such as non-axisymmetric endwall contouring, blade tip leakage mitigation, leading edge fillets and other optimization driven aerodynamic surface modifications.

II. Experimental Facility

The Axial Flow Turbine Research Facility (AFTRF) installed at the Turbomachinery Aero-Heat Transfer Laboratory of the Pennsylvania State University is a low speed, single-stage, cold flow turbine having a diameter of 91.7 cm. Table 1 summarizes the design performance parameters of the turbine facility and the design features are shown in Table 2. The detailed description and characteristics of the AFTRF can be found in Lakshminarayana, Camci, Halliwell and Zaccaria [12] and Camci [13]. The facility is driven by four stages of axial suction fans located downstream of the turbine rotor section after an outlet guide vane assembly. The speed of the rotor is controlled by a power absorbing eddy-current brake for constant speed operation. The inlet section has a bell-mouth shape followed by the *NGV* row and the rotor blades. A sketch of the AFTRF is given in Fig.1. There are 23 *NGV*'s and 29 rotor blades followed by the exit guide vanes. The operating point of the turbine, especially the flow coefficient can be altered by slightly modifying the axial position a movable throttle valve at the exit of the facility. The turbine stage is instrumented for high spatial resolution aerodynamic probe traversers that can be located upstream of the *NGV*, intrastage zone and at the exit of the rotor. The current aerodynamic loss results are presented in the form of a non-dimensional loss coefficient C_{Pt} at just downstream of the *NGV* trailing edge at $x/c=1.05$. Sub-miniature aerodynamic/aerothermal probes can be traversed in the circumferential direction. The measurements obtained in the rotating frame of reference in AFTRF could be transmitted to the stationary computer system via a 150 channel coin&brush type slip ring unit. Probe traversing is also possible in the rotating frame of reference for relative flow measurements. A sub-miniature five hole probe was used at

just downstream of the *NGV* at $x/c = 1.05$ for the high resolution measurements of radial, circumferential and axial mean velocity components, in addition to static and total pressures.

III. Computational Features

The viscous flow simulations in this paper are carried out by the general purpose finite-volume solver Ansys CFX. The three-dimensional compressible RANS flow equations are solved for steady-state air flow around *NGV* airfoils. This specific study does not include the rotor simulation, and hence, the vane-rotor interaction is not investigated at this stage. Rotationally periodic boundary conditions are applied on the side walls of the computational domain defined around the airfoils. A no-slip, adiabatic wall is selected for vane, hub and casing boundaries. For the inlet boundary, experimental flow conditions measured in-house at one axial chord upstream of the *NGV* are adapted [14]. The measured velocity magnitude and the turbulent kinetic energy distribution along the span at the inlet is shown in Fig 2. The total pressure value given as the inlet boundary condition is calculated from the measured velocity distribution. The inlet total pressure at the entrance to the bellmouth section of the AFTRF where velocity magnitude is negligible is atmospheric. Total temperature at the inlet is 298.15 K. At the outlet boundary, the experimentally determined mass flow rate value is specified. The uncertainty estimates for the experimental data are provided in Appendix-B.

Two-equation SST $k-\omega$ turbulence model of Menter [15] is selected for all simulations in this study. This turbulence model is widely used by many researchers to predict turbine secondary flows. One of the recent studies of a turbine blade simulation with this turbulence model is discussed in Levchenya et al. [16]. The flow over an uncooled turbine *NGV* or blade can be transitional over significant lengths on airfoil surfaces, [17]. It is concluded in the past literature that the transition on an *NGV* aerodynamic surface is mainly affected by the free-stream turbulence level originating from the combustor, x Reynolds number, pressure gradient, type of surface curvature and surface roughness conditions. It was previously observed that the influence of heat transfer, surface curvature, surface roughness, and the compressibility on transition are not as much as that of free-stream turbulence level. Denton [10] argues that an inaccurate specification of the transition point, instead of predicting it within the calculation, may lead to weak quantification of aerodynamic losses and turbine efficiency. Many recent researchers tried to predict transition within the framework of two equation turbulence models. Another approach is to employ empirical correlations as transition models. The Gamma-Re-Theta model employed in the current transitional flow predictions uses a built-in correlation. In this model two extra transport equations are solved, one for the intermittency (γ) and the other for momentum thickness Reynolds number ($Re_{\theta t}$). In references from [18] to [20], Menter, Langtry et al. validated the current SST turbulence

model with this correlation for various transitional flow cases. Throughout this paper, transitional flow simulations with both unstructured and structured grids will be discussed. Unstructured mesh is an automated grid generation that needs little user effort. The 2D grid structure on the solid boundaries are created first and inside of the computational volume is filled arbitrarily with unstructured tetrahedra cells in 3D. On the other hand, a structured grid has hexahedral elements which are created in an orderly pattern within the computational volume. The user can easily modify grid density at the selected regions of the flow such as wake of a blade, secondary flow areas, boundary layers and junction flows. The current investigation also considers the non-negligible influence of corner fillets at the airfoil/endwall junction areas.

IV. Discussion of Computational Results and Comparisons Against Experimental Results

IV.1 Influence of Grid Generation and Transitional Flow Modeling: Past computational simulation studies dealing with the predictability of aerodynamic losses in turbine passages used various grid generation strategies. Although the static pressure distributions and velocity magnitudes over aerodynamic surfaces were computationally recovered effectively, the predictability of viscous losses in turbine stages was not a topic of immediate success for a while. It seemed that a good combination of computational scheme, grid quality, turbulence modeling, transitional flow modeling and geometrical fidelity of the passage were simultaneously needed for successful aerodynamic loss simulations. The aerodynamic losses usually represented as a non-dimensional total pressure loss coefficient can also be viewed as the sum of the squares of the x, y and z gradients of each mean velocity component. A good simulation of the losses at a specific location does not only require a good prediction of the velocity components but also their spatial gradients. These velocity component gradients are also squared and summed together in an effort to define the dissipative/viscous losses. This approach is consistent with the idea that viscous losses occurring in turbine internal flows will also directly scale with the dissipation function that is a significant part of thermal energy equation/budget. Therefore every effort to minimize the uncertainties in the determination of spatial velocity gradients, their squares and their sum should be made. A good aerodynamic loss prediction requires highly accurate mean flow computations in boundary layers of the airfoil surfaces, endwall boundary layers, *NGV* wakes, secondary flows, corner vortices and interaction of all of the influencing parameters listed. The computation should also have the capability to resolve laminar, transitional and turbulent flow zones that are appearing simultaneously in the *NGV* flow system. In an effort to reduce some of the grid induced uncertainties throughout this study, the flow simulations with both unstructured and structured grids will be

discussed. An unstructured mesh is easy to implement in three-dimensional flows especially in internal passages with complex geometries. For instance, flow through an *NGV* passage could introduce some difficulty in mesh generation because of the vane geometry and the high turning angle of the passage. The two-dimensional mesh on the boundaries are created first and inside of the computational volume is filled arbitrarily with tetrahedra. However, arbitrariness of the tetrahedron cells requires additional flow solver time and computational memory for the connection of the non-orderly created neighboring cells. Moreover, the tetrahedron cells are insufficient in capturing the flow physics within the boundary layer and other high shear containing complex flow zones such as the wake region and secondary flow zones. Prisms should be used within the boundary layer to better resolve the near wall flow physics. On the other hand, a structured grid has hexahedral elements, which are created in an orderly pattern within the computational volume. User can easily modify grid density at the selected specific regions of the flow. The drawback of this method for complex geometries is in the fact that, it is very difficult to form a single block structured mesh. Users should split the computational domain into several blocks, which is called multi-block structured mesh generation.

IV.2 Unstructured Grid Generation: The unstructured grid generation scheme in this study involves two steps. First step is to mesh the boundaries of the whole domain. Gambit is used as a general purpose surface mesh generator. An example of this boundary grid is depicted in Fig.3. As the second step, this surface mesh is imported in Tgrid. Then, prism layers are developed from this boundary mesh perpendicular to the walls. It is crucial to use prisms to resolve the near wall gradients. The crossflows within the *NGV* passage are mainly due to the velocity magnitude differences within the incoming endwall boundary layer and strong turning in the *NGV* passage. The momentum deficit in the inlet endwall boundary layers tend to roll into secondary flows that are significant "aerodynamic-loss-generating" flow systems in the passage. If a proper grid resolution near the walls and secondary flow dominated areas is not achieved, then the simulation results will diverge from the experimental results.

To examine the effect of the number of prism layers created, the total pressure coefficient C_{pt} , is compared at the *NGV* exit plane located at $x/c = 1.05$, as shown in Fig.4 by the dashed line drawn parallel to the *NGV* trailing edge. Two different unstructured mesh results are presented in Fig.5. These C_{pt} contours are plotted up to 20% span of the vane. To clarify the position of these contour plots, it should be pointed out that the flow to the left of wake region contains the suction side boundary layer of the vane airfoil. A strong vortical region containing the passage vortex and the pressure side leg of the horseshoe vortex is also to the right of the *NGV* airfoil/endwall junction. Note that, Fig.5a and Fig.5b do not have the same number of mesh sizes. The reason is, when comparing these two cases, all the parameters within Tgrid are kept constant (*i.e.* boundary mesh, $y^+ < 1$, growth ratio of the tetrahedra within the volume), except the number

of prism layers. The importance of resolving the near wall grid is clear as shown in Fig.5b. The core of the secondary flow and the separation of the secondary flows from the endwall is well captured. The spanwise distribution of the circumferentially mass-averaged total pressure coefficient is compared to AFTRF measurements in Fig.5c. The one with tall prism layers qualitatively predicts the secondary flow areas, but there is still an offset from the experimental data. The wake is not predicted well, that is due to the coarse mesh in that region. The secondary flow region is not distinguishable in short prism layer results. The endwall loss and the secondary flow loss is mixed to each other. This study showed that when using an unstructured mesh, the prism layer plays an important role in calculating the gradients within the boundary layer.

After investigating the influence of prism layers, two more unstructured meshes are examined with tall prism layers. Boundary mesh is the same with the ones used above. Tgrid is an automatic mesh generator that fills the computational volume with tetrahedra using a specified growth ratio. The growth ratio defines the expanding of the tetrahedron cells starting from the boundary mesh. The next unstructured grid has $y^+ \sim 15$ at the first grid point near the wall and a default growth ratio of 1.6 resulting in total of 2 million cells. The C_{pt} contours in Fig.6a (2 million cells) show that the core of the secondary flow region is shifted up in the spanwise direction. The minimum value of C_{pt} is around -2.2, whereas it is around -2.8 in Fig.5b. Additionally, the secondary flow area in Fig.6a is wider both in circumferential and spanwise direction. The pressure side of the wake is still not simulated properly. The wake near the pressure side is unnecessarily spilled towards the core flow because of the relatively coarse grid structure. It is concluded that, more cells are needed in the domain, especially near the pressure side of the wake and in the secondary flow zone near the suction side at the *NGV* exit. Moreover, $y^+ < 1$ at the first grid point is an essential grid resolution near the wall to calculate the flow physics within the boundary layer especially in transitional boundary layers and heat transfer problems. The wall function approach is not suitable according to the discussion of Oberkampf and Blottner [9]. Even though the wall function approach reduces the size of the grid required, the velocity gradients may not be captured accurately in the logarithmic layer, especially when there is separation near the wall.

The last unstructured grid as shown in Fig.6b has $y^+ < 1$ at the first grid point near the wall with a growth ratio of 1.1, having 6.5 million cells in total. The total pressure contours are smoother, and the wake is well predicted. The circumferentially mass-averaged distribution of C_{pt} along the span is depicted in Fig.6c. The core of the secondary flow region is predicted closer to the wall when compared to the experimental data. Even though this 6.5 million-cell grid simulates the *NGV* passage flow properly, the necessity of large computational memory and time concerns come into the picture. The authors of this paper decided to switch to body fitted block structured grid for time efficient and well

predicted computational simulations. It should be noted that optimal grid sizes mentioned in this paper were tested in only one specific computational flow solver system. The structured grid based flow simulations will be introduced and discussed in the next section.

IV.3 Structured Grid Analysis with Transitional Flow Modeling: A grid independence study is performed with different resolutions of the structured grid. As noted previously, for complex geometries, it may be beneficial to use a multi-block grid strategy to create a mesh almost orthogonal to the boundaries. GridPro is selected as the grid generator. A sample grid of the *NGV* is shown in Fig.7. From the previous section it was learned that the near wall grid resolution is important, therefore, $y^+ < 1$ is assured with the structured grid as well.

The first results with a structured grid are obtained with fully turbulent flow assumption starting from the inlet of the computational domain. Transition criteria is not taken into account, initially. Four different structured mesh sizes are compared, namely 0.6, 1.0, 2.0, and 4.3 million cells. The circumferentially mass-averaged total pressure coefficient distribution at the *NGV* exit is plotted in Fig.8. The first important item to notice in this figure is that the profile losses of the *NGV* are not accurately predicted. For the 2.0 and 4.3 million cell grids the typical deviation is around 50% and for 0.6 and 1.0 million cell grids it is around 100% when computations are compared to AFTRF experiments. These deviations appear to be very large, but note that, the C_{pt} value at the midspan is approximately -0.05. As for the grid independence, it is clear from the figure that 2.0 and 4.3 million cells are giving the similar results. The aerodynamic losses are over-predicted especially in the profile loss zone. Whereas, for the 0.6 and 1.0 million cell grids, the over-prediction of the total pressure is much more exaggerated. For instance, from the hub to 7% span location, there is a $\Delta C_{pt} = 0.05$ between the coarse mesh result (0.6 and 1.0 millions cells) and fine mesh result (2.0 and 4.3 million mesh). Although the computational results in this figure provide an important information on grid independence, the authors still think that this is not a reliable CFD prediction for future calculations. The simulations seem to be grid independent after a grid size of 2 million cells, however the accuracy of these seemingly grid independent simulations are questionable.

Mayle [17] states that the flow over an uncooled turbine *NGV* or blade can be transitional. The transition phenomenon in gas turbines is thoroughly discussed in [17]. It is concluded that the transition is mainly dominated by the free-stream turbulence level, x Reynolds number, pressure gradient, type of surface curvature and unsteady wake passing in certain turbine stages. The influence of heat transfer, surface curvature, surface roughness, and the compressibility on the transition are not as much as free-stream turbulence level. Denton [10] argues that an inaccurate specification of the transition point, instead of predicting it within the calculation, may lead to weak quantification of

turbine efficiency. Many researchers tried to predict transition within the two equation turbulence models. Another approach is to employ empirical correlations as transition models. The Gamma-Re-Theta model in the general purpose solver CFX uses a built-in correlation. In this model two extra transport equations are solved, one for the intermittency (γ) and the other for momentum thickness Reynolds number ($Re_{\theta t}$). SST turbulence model with this correlation is validated for various transitional flow cases [18-20]. In the present study, the Gamma-Re-Theta model is selected as the transitional flow model. The same type of structured grids as discussed in the previous paragraphs are used to observe the transitional effects throughout the computations. The circumferentially averaged total pressure coefficient distribution in the spanwise direction at *NGV* exit plane is presented in Fig.9. The grids with 2.0 and 4.3 million cells predict C_{pt} very close to experimental data along the wake and in the secondary flow zone near the hub. One should notice that the *NGV* exit flow measurements near the casing above % 80 span carry slightly more uncertainty because of the probe insertion slot related flow disturbances on the turbine casing at the exit of the *NGV*. This paper consistently uses the near hub aerodynamic loss measurements for comparative purposes because of seemingly higher computational fidelity in the spanwise region below % 80 span. It is apparent that the computations with the grids with 0.6 and 1.0 million cells are not capable of capturing the wake profile and the profile losses. There is again a difference of $\Delta C_{pt} = 0.05$ up to 60 % span between the coarse (0.6 and 1.0 million) and fine mesh (2.0 and 4.3 million). There is also a relatively weak comparison for all structured grids above 90% span of the vane. The main reason for this mismatch is again the existence of the open casing slot on the experimental facility that the probe could traverse in circumferential direction. Although a significant technical effort is made to minimize this slot influence, a complete elimination of its influence is not the case. In CFD calculations, this slot is not taken into account, and therefore the total pressure loss is calculated somewhat less than the experimental data.

The midspan static pressure coefficient distributions on the blade airfoil surfaces are shown in Fig.10. All of the structured grid configurations calculate similar C_p values and they are all in very good agreement with the experimental measurement. Note that, very close to the trailing edge region, the C_p distribution indicates a negative loading. This behavior is well described by Denton [10]. When a very fine grid is used near the trailing edge, the flow separation is delayed, which is supposed to be at the pressure surface and trailing edge junction. The flow remains reattached and accelerates around the trailing edge, causing a non-negligible pressure drop.

One of the goals of this study is to capture the secondary flows in the *NGV* passage and the related total pressure loss at the *NGV* exit. Fig.10 suggests that even a 0.6 million cell grid structure accurately predicts the static pressure coefficient at midspan. However, it is obvious from Fig.9 that the calculation is grid dependent for the total pressure

coefficient prediction below 2.0 million cells. For computational time consumption considerations and the effective usage of computer resources, the authors of this paper selected the 2.0 million cell grid structure as a sufficient mesh resolution for properly resolving the flow physics.

IV.4 Influence of Corner Fillet: The results of the structured grids previously discussed did not include the corner fillet. They were all computed using 90 ° sharp corners. It is very rare in the open literature to find turbine passage computations taking into account the influence of corner fillets. This is, in other words, the fillet at the junction of the vane airfoil and the hub endwall. Most actual turbine passage geometries have corner fillets of measurable fillet radius. In actual AFTRF experiments, this fillet was there, and all of the measured data includes the effect of this fillet. Germain et al. [21] also states that the fillet has an important role in total pressure coefficient distribution. To investigate the influence of corner fillet in CFD calculations, a structured grid is generated in such a way that fillet is also taken into account. The structured grid, including the corner fillet, is shown in Fig.7. GridPro is capable of mapping the grid to such fillets and creating an orthogonal mesh. Clearly, the corner fillet changes the distribution of the C_{pt} along the span as shown in Fig.11. From 4% to 12% span, the distribution is shifted up approximately 1% of the vane height in the spanwise direction. Above 12% of the span both cases calculated similar values. The results with corner fillet, especially within the secondary flow region, came out to be in more agreement with the experimental data than the results without corner fillet.

The contour plots of total pressure coefficient at *NGV* exit plane for experimental AFTRF measurement and CFD calculation are given in Figs.12a and 12b. The C_{pt} values in Fig.12a are positive due to the definition of the expression given by [11]. The total pressure coefficient was defined as $\frac{P_{01} - P_{02}}{0.5 \rho U_m^2}$ which had a reverse sign of our definition. When comparing these two figures, readers should keep in mind that the contour levels and their increments are the same except the sign. Qualitatively, the contour lines show similar behavior. The minimum local C_{pt} value for experimental result is around -1.9, whereas, for computational result it is around -2.8. The circumferentially mass-averaged values are in very good agreement above 12 % span with each other as was shown in Fig.11. The influence of the corner fillet is obvious near the hub area, up to 12 % span. However, the computations with fillet and without fillet are about the same above 12 % span indicating that the influence of the fillet is only observable near the hub.

The experimental AFTRF NGV exit static pressure distribution along the span is given in Fig.13. The mass-averaged experimental distribution of Zaccaria et al. [11], [12] is somewhat scattered along the span within the quoted experimental uncertainty band. Nevertheless, the computational result is following the meanline of the scattered data.

Moreover, the three components of computed velocity, namely axial, radial and circumferential, and the velocity magnitude are plotted in Fig.14. All the data, except the radial component, are in very good agreement with experimental measurements obtained in AFTRF. But note that, the non-dimensional radial component is around zero, and the difference of $V/U_m \approx 0.05$ corresponds to a value of approximately 2.5 m/s.

IV.5 Numerical Flow Visualization: Flow visualization results extracted from 3D and high resolution viscous flow computations are presented in Fig.15. The comparison between the streamlines near the endwall and at the midspan is shown in Figs.15a and 15b. Clearly, the existence of the endwall boundary layer momentum deficit changes the paths of the streamlines which are closer to the hub endwall. The flow particles with lower velocity magnitudes on the pressure side of the passage tend to move towards the suction side of the vane. That trend is not seen near the midspan. The flow trajectories smoothly follow the vane boundaries without any deflection. The cross flows in the blade to blade planes especially near the hub and the existence of the NGV leading edge generated horse-shoe vortices form a typical aerodynamic loss core appearing near the suction surface as shown in Figure 12. Both computations and measurements clearly mark this high aerodynamic loss region.

To see the effect of endwall boundary layer in more detail, infinitesimal small mass containing particles are released on a vertical line from hub to 5% span at the inlet boundary, as shown in Figs.15c and 15d. The streamlines/pathlines with red and yellow colors are directed to the suction side, green and light blue colored ones go to the pressure side of the vane. The yellow streamlines, which are in the boundary layer with lower velocity magnitudes, change their path to the suction side near the minimum pressure point and rise on the vane surface. Meanwhile, the red ones follow their trajectory with minimum deflection. The pressure side streamlines have similar trend. Again, the light blue ones within the boundary layer are deflected towards the suction side surface. But note that, the green streamlines which are released just above the light blue ones, tend to fill the gap of the deflected light blue streamlines. As the flow approaches to the end of the passage, both the green and the light blue ones move beneath the red streamlines and meet with the yellow ones.

The vortex core regions are presented in Fig.16. Q -Criterion is selected as the method to isolate/visualize secondary flows. It is defined as the second invariant of the velocity gradient tensor. This method is developed by Hunt et al. [22], and the positive values of Q indicates vortex regions. There are two secondary flow regions on the suction side surface of the vane; one closer to the hub, and the other closer to the casing. The horseshoe vortex forms two significant parts as it is wrapped around the leading edge of the NGV, suction side leg and the pressure side leg. The suction side leg reattaches to the suction surface near the minimum pressure point, and rises on the surface through the midspan. The

effect of crossflows from the pressure side to the suction side is clear on the casing. There are two distinct secondary flow structures near the casing. One is the suction side leg of the horseshoe vortex, which moved towards the midspan, and the other one is generated from the crossflows. The current computations are able to represent the aerodynamic loss of this *NGV* flow system with good accuracy when proper precautions are taken in defining the actual boundary conditions, grid system, the fillet geometry and transitional flow features.

V. Conclusions

Although experiments provide valuable results in an actual turbine passage, it is still time consuming and expensive to set up full scale turbine aero-thermal experiments under actual operating conditions at a high spatial resolution. This investigation shows that the highly three-dimensional secondary flows in a turbine *NGV* passage can be effectively quantified by computational fluid dynamics not only for static pressure and velocity vector magnitudes but also for viscous/dissipative losses frequently termed as aerodynamic losses.

The experimentally obtained AFTRF viscous flow data set and the *NGV* geometrical details used in the assessment and validation of the current computational results are also available from the authors of this paper. Existence of a well defined turbine stage geometry and associated experimental data set is helpful for validating a viscous flow solver to be implemented in any turbomachinery design system.

From the unstructured grid results, it was concluded that the number of prism layers influences the calculation of the gradients within the boundary layer. Additionally, a high grid resolution near the wall was suggested. Another important conclusion from the unstructured grid study was that a finer mesh was needed around the wake and secondary flow regions. As the number of mesh cells was increased, the prediction of the total pressure coefficient values gradually approached to the experimental data. On the other hand, increasing the number of mesh cells brought on other difficulties such as a larger memory demand and an increase in overall computational time. Hence, the authors of this paper suggested the use of block structured body-fitted grids for reasonably accurate CFD simulation of *NGV* flows in an HP turbine stage. A structured grid is computationally more efficient whilst giving good validation with experimental data.

The fully turbulent computations over-predicted the profile losses or the wake loss of the *NGV*. Knowing that the suction side of this uncooled *NGV* airfoil may have a long laminar flow zone after the leading edge, the authors decided

to simulate the transitional flow features in the computations. Therefore, transitional flow physics were taken into account, and hence, wake profile and profile losses were successfully simulated when compared to experiments.

Another aspect of the structured grid study was the investigation of the corner fillet effect. It was shown that the secondary flow region was shifted upwards about 1% vane span in the spanwise direction, resulting in a better agreement with the experimental total pressure measurement at the *NGV* exit. The computed static pressure coefficient, the three velocity components, and the velocity magnitude at the *NGV* exit showed very good correspondence with the AFTRF aerodynamic experiments performed in our laboratory.

This paper showed that the current computational approach was successful in simulating our turbine experiments performed in the large scale, low speed rotating turbine stage AFTRF operated under full Re number simulation. The non-dimensional aerodynamic loading distributions on rotating blades were also well simulated. The experimentally obtained aerodynamic losses in the *NGV* passage of the current HP stage were successfully obtained from the computational simulations. The *NGV* wake, secondary flow structure, and hub endwall boundary layer were all effectively simulated. The general simulation approach developed in this paper forms a solid foundation for the development of new *NGV* aerodynamic loss reduction features such as non-axisymmetric endwall contouring, leading edge fillets and other optimization driven aerodynamic surface modifications.

The current computations are able to represent the aerodynamic loss of this *NGV* flow system with good accuracy only when proper precautions are taken into account in defining the actual boundary conditions, grid system, the fillet geometry and transitional flow features.

Appendix A: AFTRF Nozzle Guide Vane Geometry

The five-section *NGV* profile as shown in Figure 17 shows the three-dimensional solid model of the vane geometry that is available to researchers who are in the need of high resolution validation geometry and data for multi-dimensional viscous flow solvers. Contact authors at cxc11@psu.edu for the geometrical details of AFTRF 3D *NGV* solid model and its 3D coordinates with well documented boundary conditions obtained from experiments.

Appendix B: Experimental Data Uncertainty

In this paper, the computational results are compared to the high resolution experimental data obtained by various researchers in AFTRF in our laboratory [11], [14]. The turbulence intensity is measured using a single sensor hot wire at one chord upstream of the *NGV* leading edge. The calculated total uncertainty for hot wire measurements is

documented as 1.9% in measured turbulence intensity. The nozzle guide vane exit flow is measured with a five hole probe. The relative uncertainty for velocities are estimated as 0.6% for V , 2.5% for V_x , 0.5% for V_θ , and 22% for V_r . The uncertainties for total pressure and static pressure are calculated as ± 30 Pa and ± 33 Pa, respectively. The relative uncertainties on the total pressure and static pressure are about 0.03% and 0.033% of total pressure at NGV exit .

Acknowledgments

The authors acknowledge the financial support provided by Siemens Energy Inc. and thank to Dr. Matthew Montgomery, Dr. Prakash Chander, Dr. Michael Crawford, Andrew Lohaus, Anthony Malandra, Ching-Pang Lee, Boris Dobrzynski, Humberto Zuniga, Ken Landis, and Dirk Nuernberger. The authors acknowledge the daily technical and financial support provided for the maintenance operation of the AFTRF by the Department of Aerospace Engineering at Penn State University. Cengiz Camci also acknowledges the support generously provided to him by TUBITAK, The Scientific and Technological Research Council of Turkey, during his sabbatical leave at Istanbul Technical University. The final editing phase of this publication would not have been materialized without TUBITAK's support. Mr. Rick Auhl, Mark Catalano and Kirk Hellen of Aerospace Engineering at Penn State provided significant technical expertise in all of our turbine runs and large scale computing efforts. The aerodynamic probe construction at the sub-miniature scale and probe traversing systems would not be possible without Mr.Harry Houtz's outstanding technical contributions.

References

- [1] Denton, J. D., *Loss Mechanisms in Turbomachines*, ASME Journal of Turbomachinery, Vol. 115, 1993, pp. 621-650.
- [2] Sieverding, C. H., *Recent Progress in the Understanding of Basic Aspects of Secondary Flows in Turbine Blade Passages*, ASME Journal of Engineering for Gas Turbines and Power, Vol. 107, No. 2, 1985, pp. 248-257.
- [3] Langston, L. S., *Secondary Flows in Axial Turbines-A Review*, Heat Transfer in Gas Turbine Systems, Annals of the New York Academy of Sciences, Vol. 934, 2001, pp. 11-26.

- [4] Hah, C., *A Navier-Stokes Analysis of Three-Dimensional Turbulent Flows Inside Turbine Blade Rows at Design and Off-Design Conditions*, ASME Journal of Engineering for Gas Turbines and Power, Vol. 106, 1984, pp. 421-429.
- [5] Moore, J. and Moore, J. G., *Performance Evaluation of Linear Turbine Cascades Using Three-Dimensional Viscous Flow Calculations*, ASME Journal of Engineering for Gas Turbines and Power, Vol. 107, 1985, pp. 969-975.
- [6] Dorney, D. J. and Davis, R. L., *Navier-Stokes Analysis of Turbine Blade Heat Transfer and Performance*, ASME Journal of Turbomachinery, Vol. 114, 1992, pp. 795-806.
- [7] Harvey, N. W., Brennan, G., Newman, D. A., and Rose, M. G., *Improving Turbine Efficiency Using Non-Axisymmetric End Walls: Validation in the Multi-Row Environment and with Low Aspect Ratio Blading*, ASME Paper No. GT-2002-30337, 2002.
- [8] Nagel, M. G. and Baier, R.-D., *Experimentally Verified Numerical Optimization of a Three-Dimensional Parametrized Turbine Vane With Nonaxisymmetric End Walls*, ASME Journal of Turbomachinery, Vol. 127, 2005, pp. 380-387.
- [9] Oberkampf, W. L. and Blottner, F. G., *Issues in Computational Fluid Dynamics Code Verification and Validation*, AIAA Journal, Vol. 36, No. 5, 1998, pp. 687-695.
- [10] Denton, J. D., *Some Limitations of Turbomachinery CFD*, ASME Paper No. GT2010-22540, 2010.
- [11] Zaccaria, M. and Lakshminarayana, B., *Investigation of Three-Dimensional Flowfield at the Exit of a Turbine Nozzle*, Journal of Propulsion and Power, Vol. 11, No. 1, January-February 1995, pp. 55-63.
- [12] Lakshminarayana, B., Camci, C., Halliwell, I., and Zaccaria, M., *Design and Development of a Turbine Research Facility to Study Rotor-Stator Interaction Effects*, International Journal of Turbo and Jet Engines, Vol. 13, 1996, pp. 155-172.
- [13] Camci, C., *Experimental and Computational Methodology for Turbine Tip De-sensitization*, VKI Lecture Series 2004-02, Turbine Blade Tip Design and Tip Clearance Treatment 2004.
- [14] Zaccaria, M . A., *An Experimental Investigation into the Steady and Unsteady Flow Field in an Axial Flow Turbine*, Ph D Thesis, The Pennsylvania State University, University Park, PA, 1994.
- [15] Menter, F. R., *Two-Equation Eddy-Viscosity Turbulence Models for Engineering Applications*, AIAA Journal, Vol. 32, No. 8, 1994, pp. 1598-1605.
- [16] Levchenya, A. M., Smirnov, E. M., and Zaytsev, D. K., *Numerical Simulation of the Endwall Heat Transfer in the Langston Cascade*, Int. Symp. on Heat Transfer in Gas Turbine Systems, 9-14 August, Antalya, Turkey 2009.

- [17] Mayle, R. E., *The Role of Laminar-Turbulent Transition in Gas Turbine Engines*, ASME Paper No. 91-GT-261, 1991.
- [18] Menter, F. R ., Langtry, R. B., Likki, S. R., Suzen, Y. B., Huang, P. G., and Völker, S., *A Correlation Based Transition Model Using Local Variables Part 1- Model Formulation*, ASME Paper No. GT2004-53452, 2004.
- [19] Langtry, R. B., Menter, F. R., Likki, S. R., Suzen, Y. B., Huang, P. G. , and Völker, S., *A Correlation Based Transition Model Using Local Variables Part 2- Test Cases and Industrial Applications*, ASME Paper No. GT2004-53454, 2004.
- [20] Langtry, R. B. and Menter, F. R., *Transition Modeling for General CFD Applications in Aeronautics*, AIAA Paper No. 2005-522, 2005.
- [21] Germain, T., Nagel, M., Raab, I., Schuepbach , P., Abhari, R. S., and Rose, M., *Improving Efficiency of a High Work Turbine Using Non-Axisymmetric Endwalls Part I: Endwall Design and Performance*, ASME Paper No. GT2008-50469, 2008.
- [22] Hunt, J. C. R., Wray, A. A., and Moin, P., *Eddies, Stream, and Convergence Zones in Turbulent Flows*, Center for Turbulence Research Rep., 1988, pp. 193-207.

Tables

Table 1. The AFTRF design performance parameters.

Inlet total temperature ($^{\circ}\text{K}$); T_{0_1}	289
Inlet total pressure (kPa); P_{0_1}	101.36
Mass flow rate (kg/s); Q	11.05
Rotational speed (rpm); N	1300
Total pressure ratio; P_{0_1}/P_{0_3}	1.0778
Total temperature ratio; T_{0_3}/T_{0_1}	0.981
Pressure drop (mmHg); $P_{0_1} - P_{0_3}$	56.04
Power (kW); P	60.6

Table 2. The AFTRF design features.

Rotor hub tip ratio	0.7269
Tip radius (m); R_{tip}	0.4582
Blade height (m); h	0.1229
Tip relative Mach number	0.24 (max)
Nozzle guide vane (tip)	
number	23
chord (m)	0.1768
spacing (m)	0.1308
turning angle	70
maximum thickness (mm)	38.81
Midspan axial chord	
nozzle (m)	0.1123
rotor (m)	0.09294
Vane Reynolds number	
based on inlet velocity	$(3 \sim 4) \times 10^5$
based on exit velocity	$(9 \sim 10) \times 10^5$

Figures

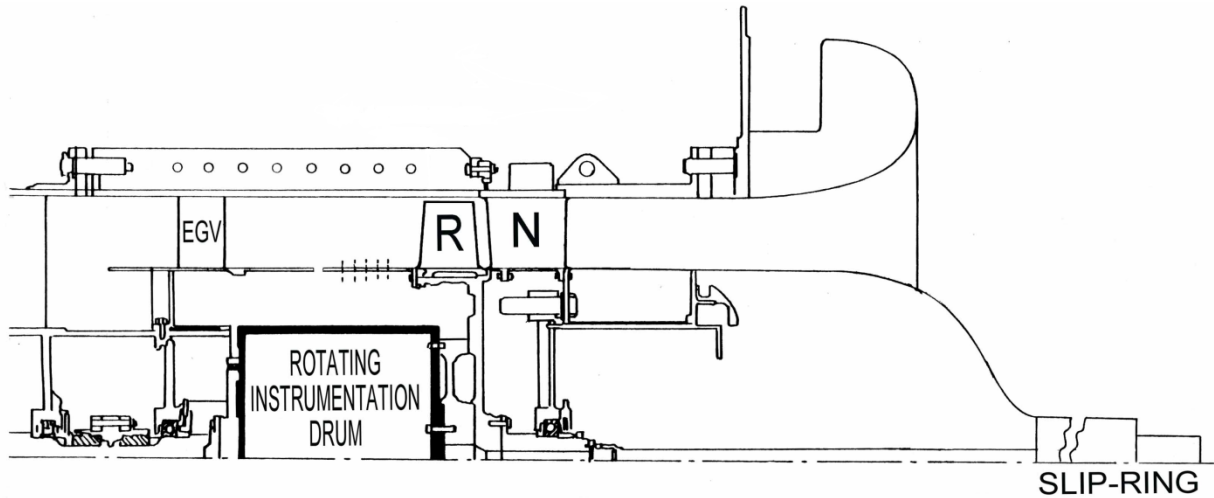


Figure 1. The rotating, large scale turbine facility sketch, Axial Flow Turbine Research Facility AFTRF.

Experimental Inlet Boundary Conditions

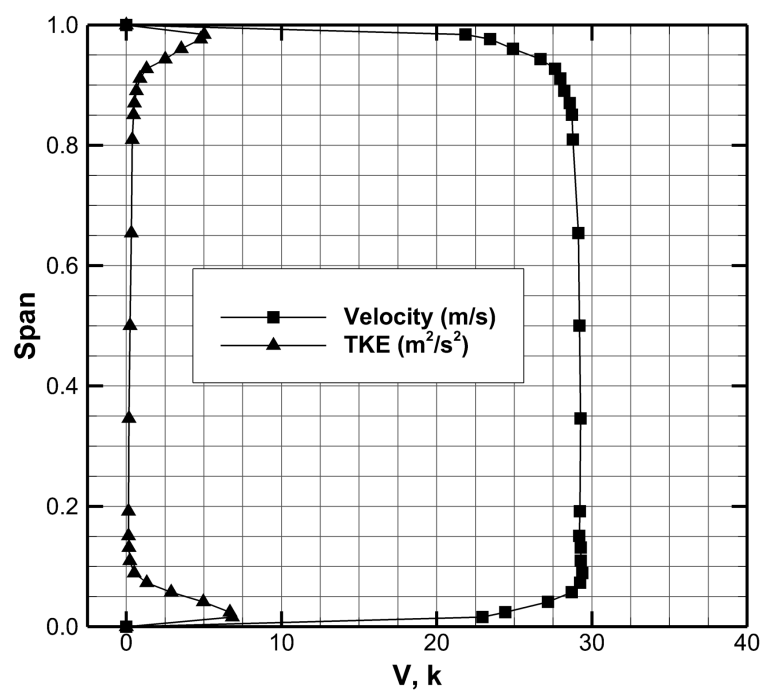


Figure 2. Experimental inlet velocity magnitude and turbulent kinetic energy distribution, measure one chord upstream of the AFTRF NGV assembly.

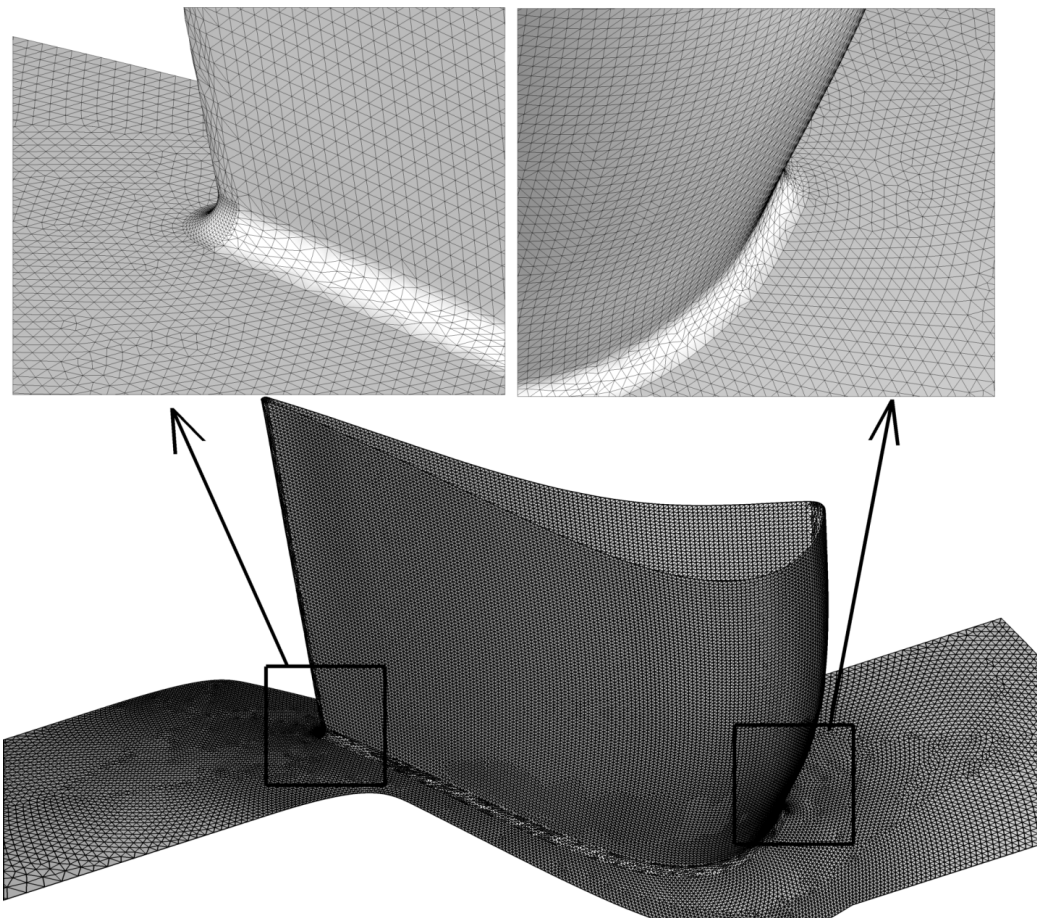


Figure 3. Unstructured grid, for the AFTRF NGV.

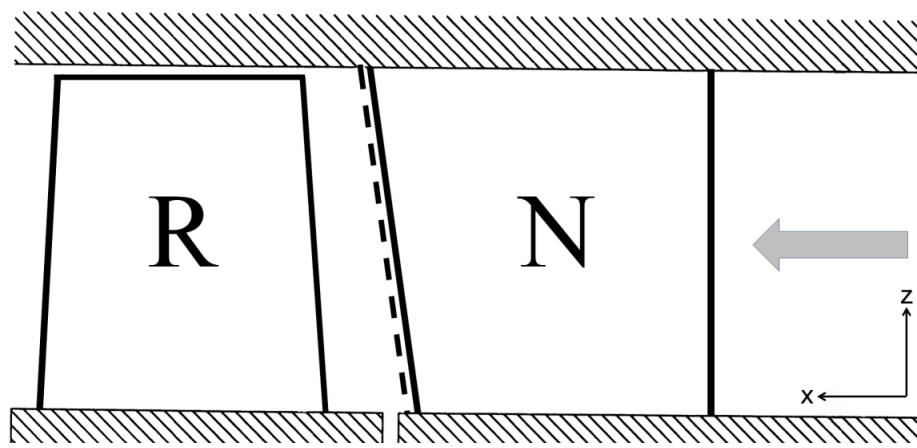
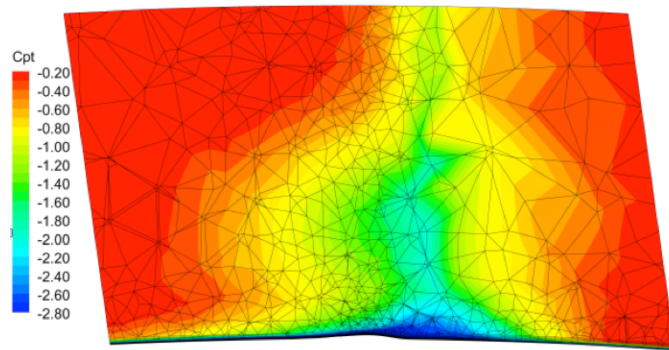
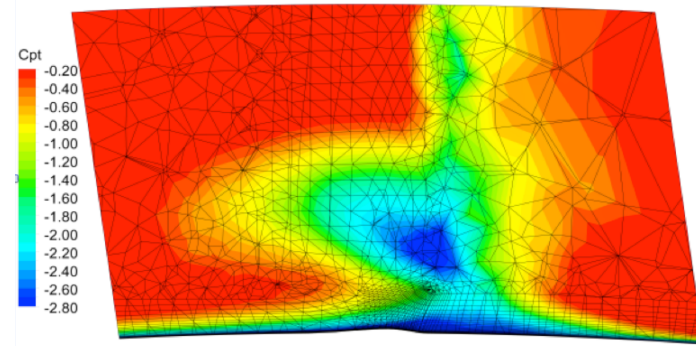


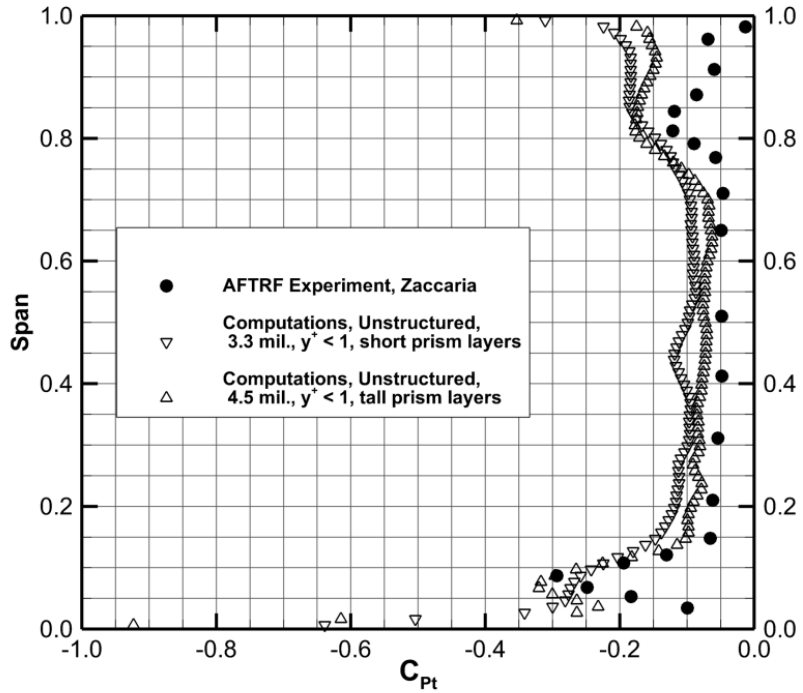
Figure 4. AFTRF, NGV exit plane definition.



(a) 3.3 million mesh cells with short prism layers, up to % 20 span measured from the hub endwall.

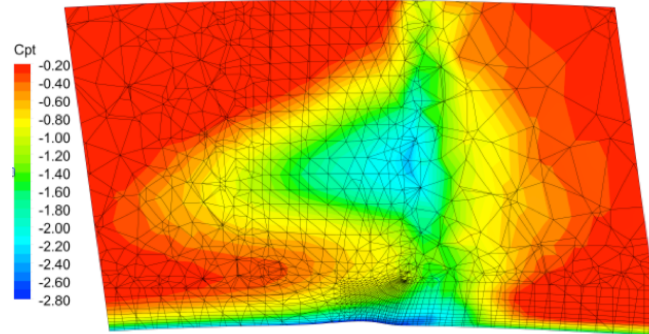


(b) 4.5 million mesh cells with tall prism layers, up to % 20 span measured from the hub endwall.

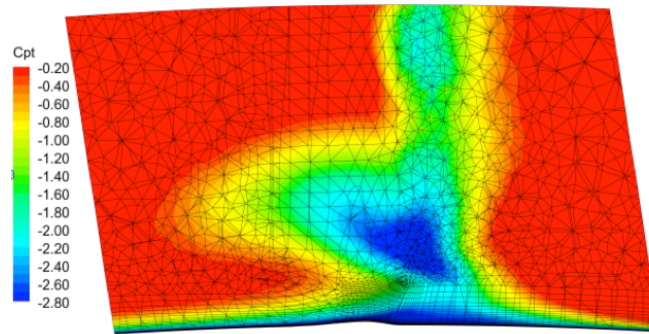


(c) Spanwise distribution of total pressure coefficient

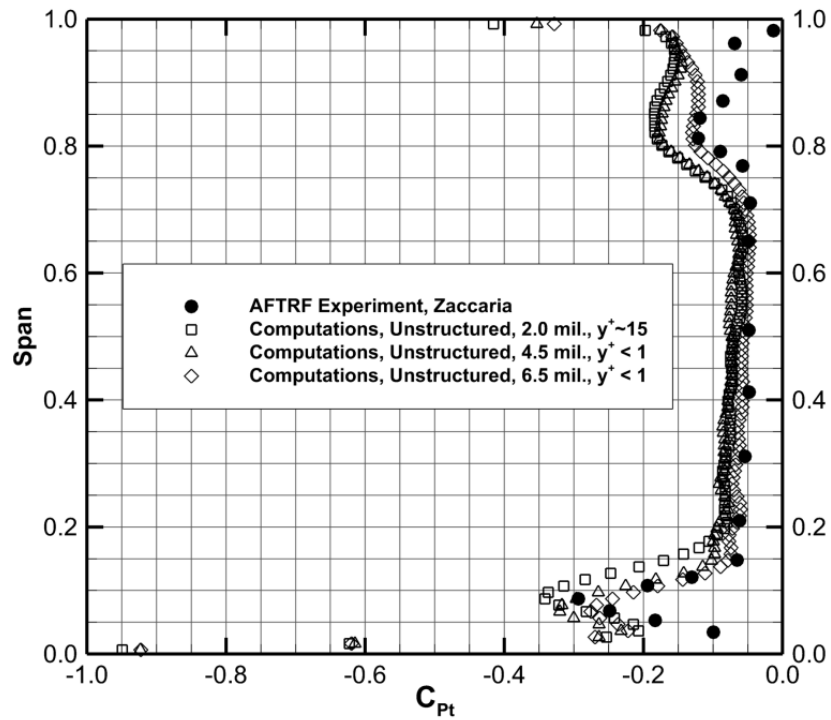
Figure 5. Prediction of total pressure loss and comparison with AFTRF experimental data [11], effect of prism layer height on unstructured mesh at NGV exit plane.



(a) 2.0 million mesh cells, up to % 20 span measured from the hub endwall.



(b) 6.5 million mesh cells, up to % 20 span measured from the hub endwall.



(c) Spanwise distribution of total pressure coefficient

Figure 6. Prediction of total pressure loss and comparison with AFTRF experimental data [11], unstructured mesh comparison at NGV exit plane.

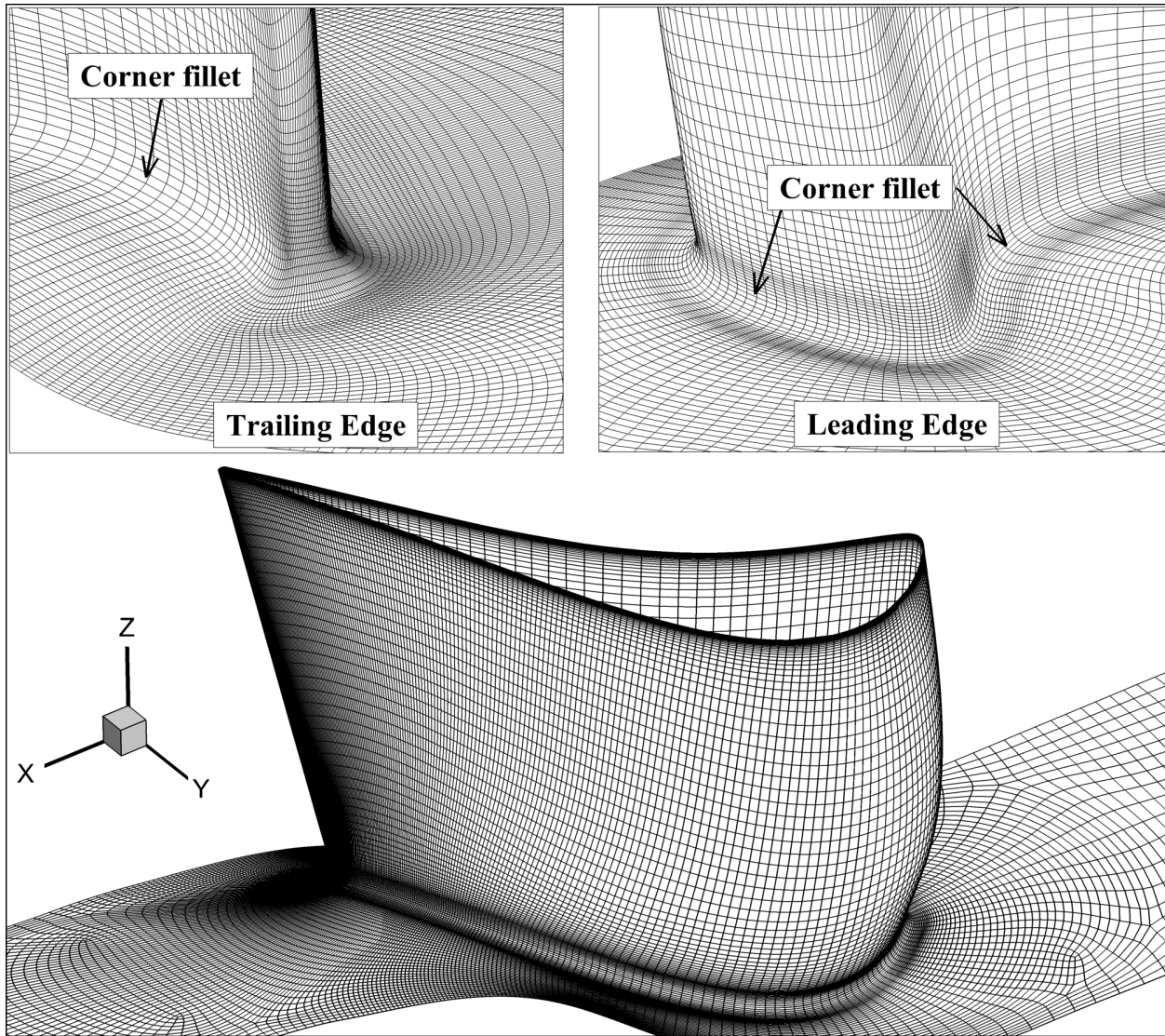


Figure 7. Block structured body-fitted mesh on AFTRF NGV surfaces.

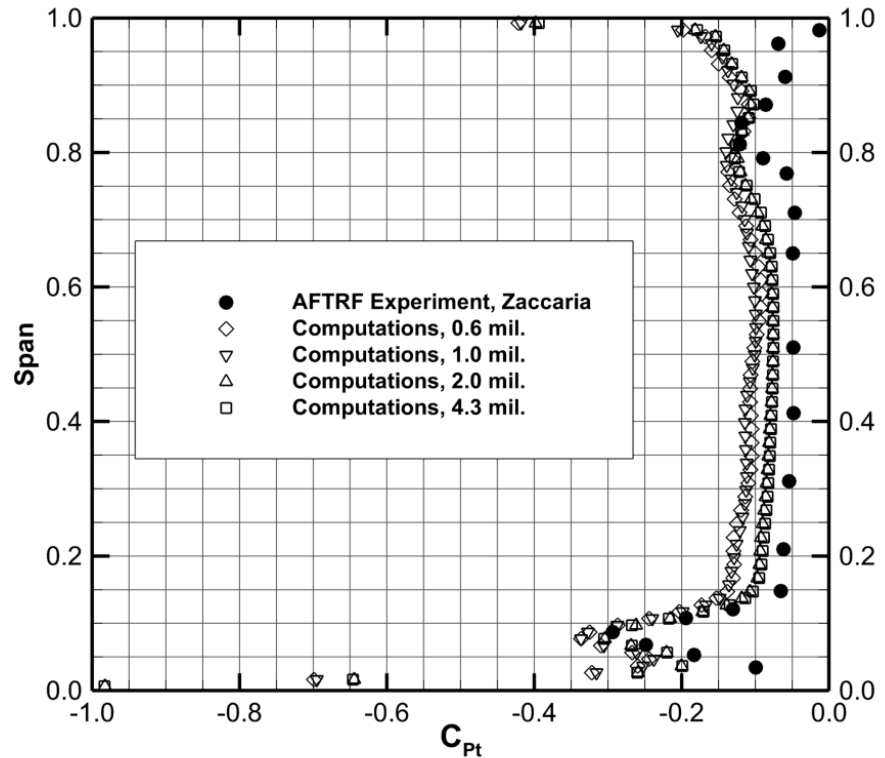


Figure 8. Grid independence study on C_{pt} at NGV exit without transition model, comparison with AFTRF experimental data [11].

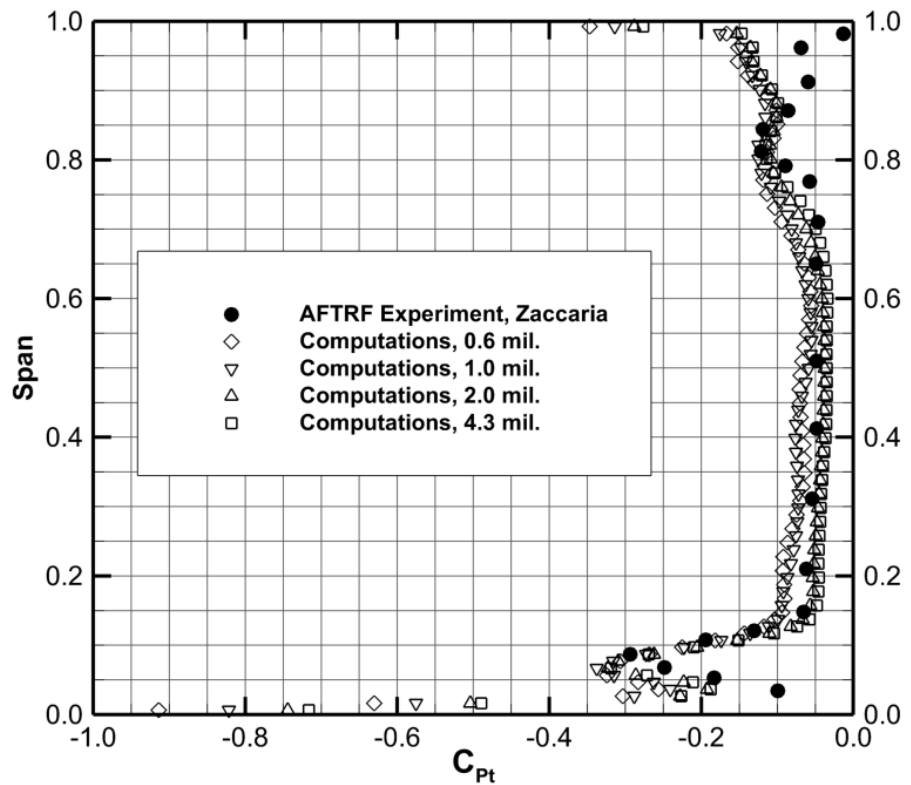


Figure 9. Grid independence study on C_{pt} at NGV exit with transition model, comparison with AFTRF experimental data [11].

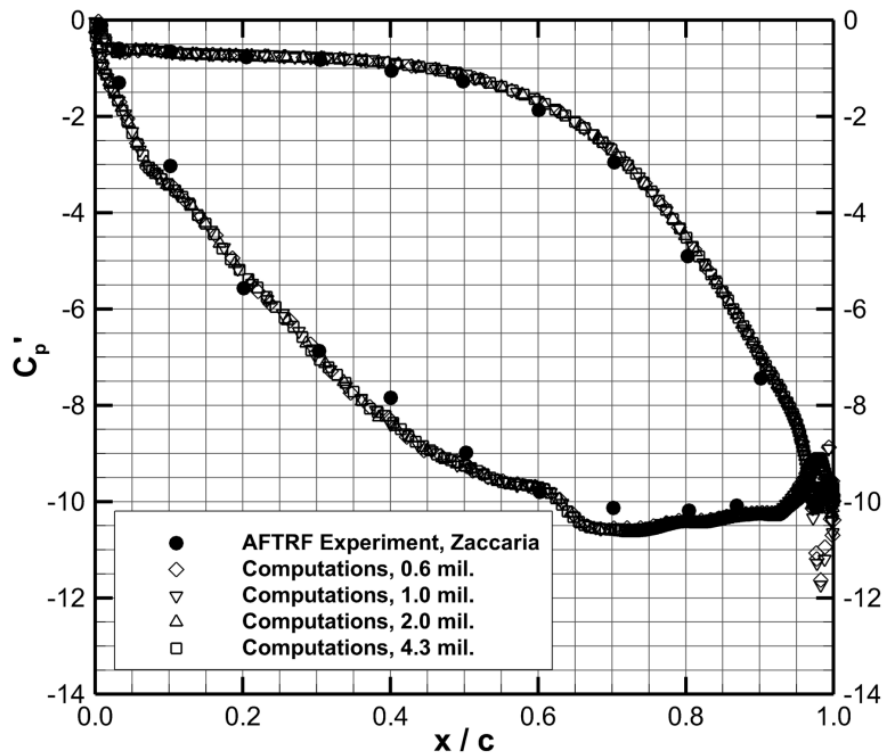


Figure 10. Grid independence study on C_p' at midspan with transition model, comparison with AFTRF experimental data [11].

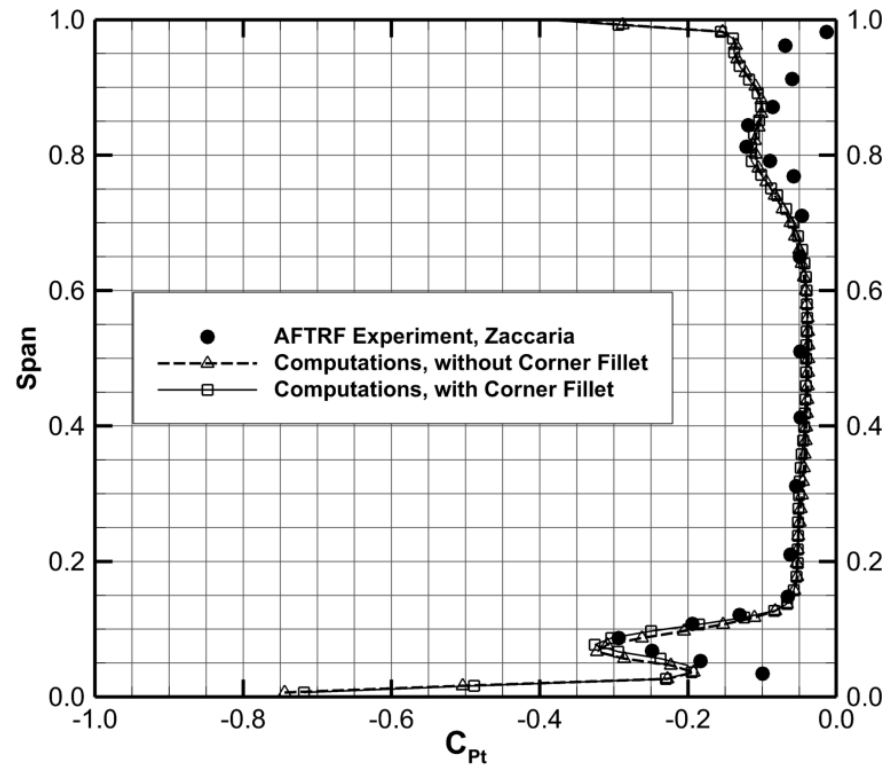
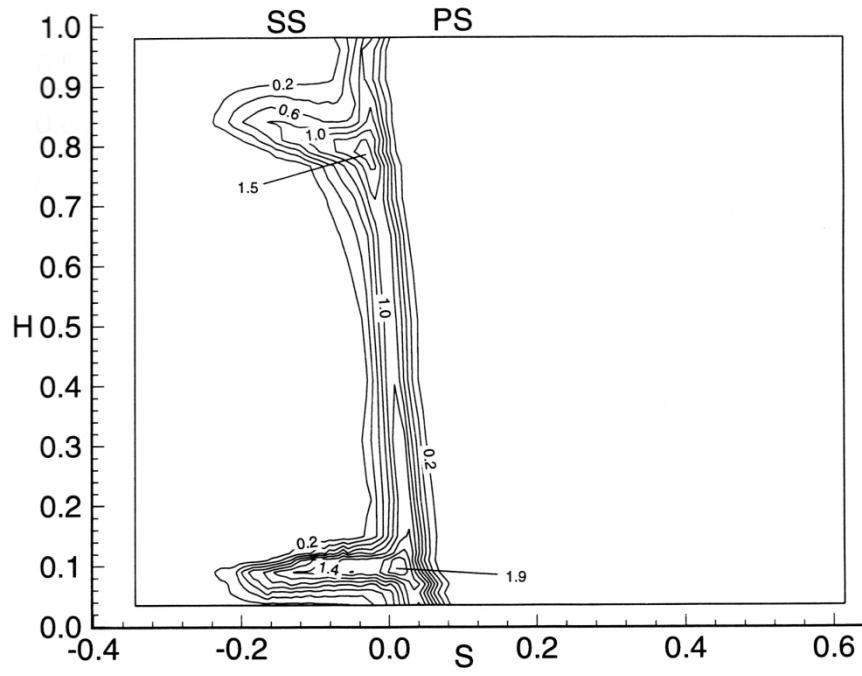
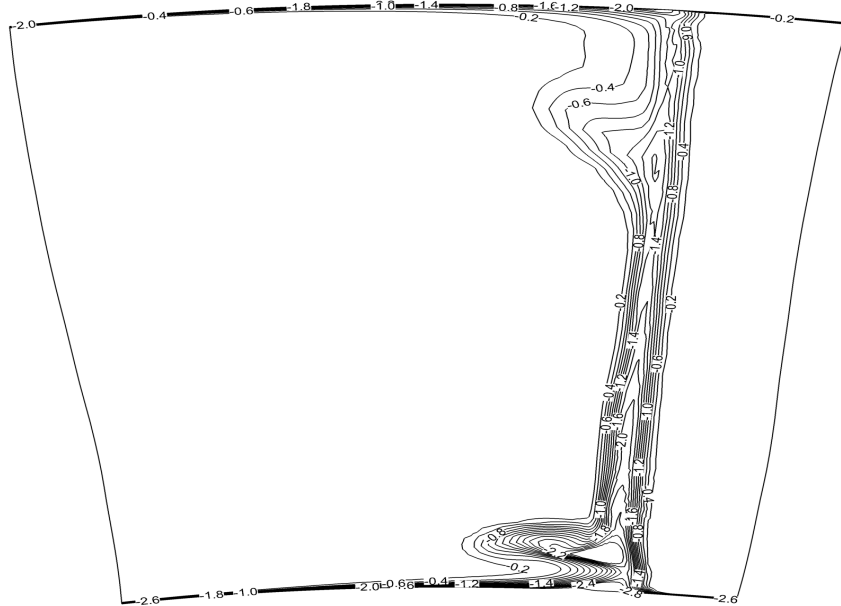


Figure 11. Effect of corner fillet, comparison with AFTRF experimental data [11].



(a) AFTRF Experiments [11], NGV exit plane measured C_{Pt} contours, $x/c = 1.05$.



(b) Current computational result, NGV exit plane C_{Pt} contours, $x/c = 1.05$.

Figure 12. NGV exit plane total pressure coefficient contours.

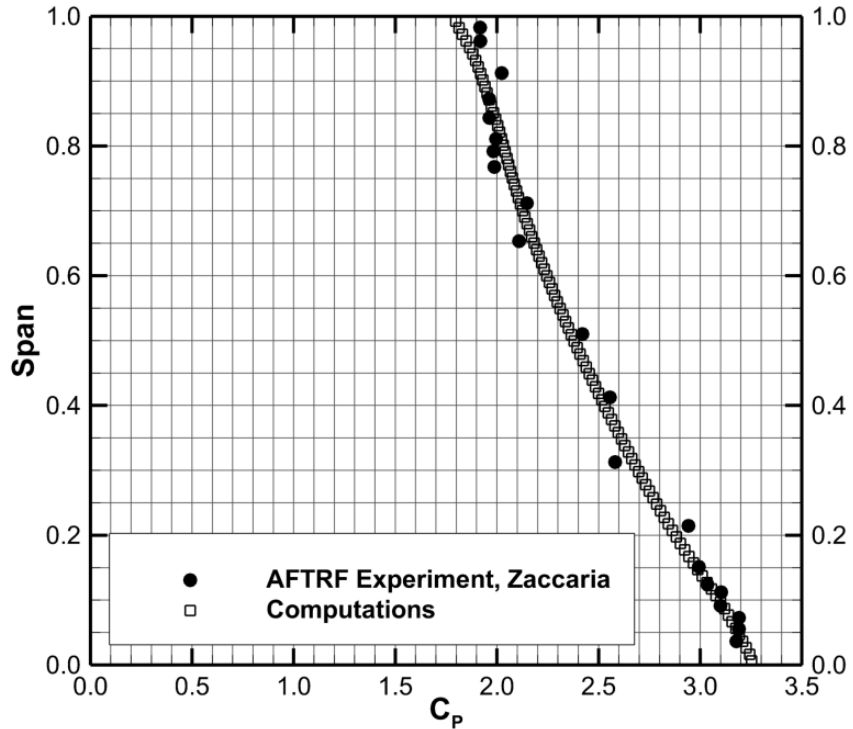


Figure 13. Computed static pressure coefficient at NGV exit plane, comparison with AFTRF experimental data [11].

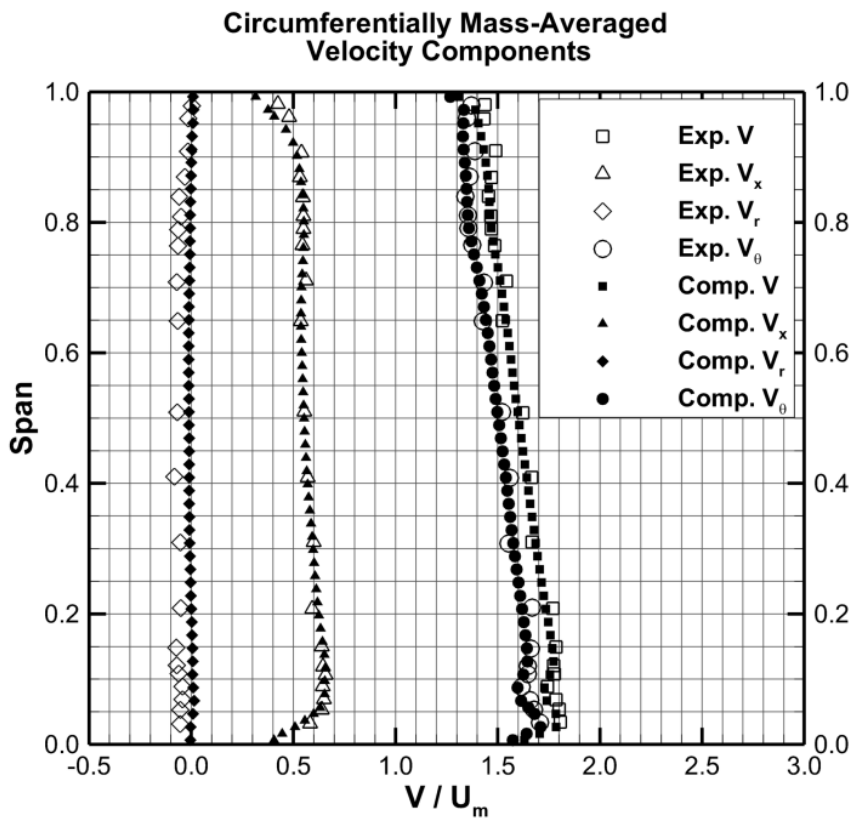


Figure 14. Velocity components at NGV exit plane, comparison with AFTRF subminiature five-hole-probe measurements [11].

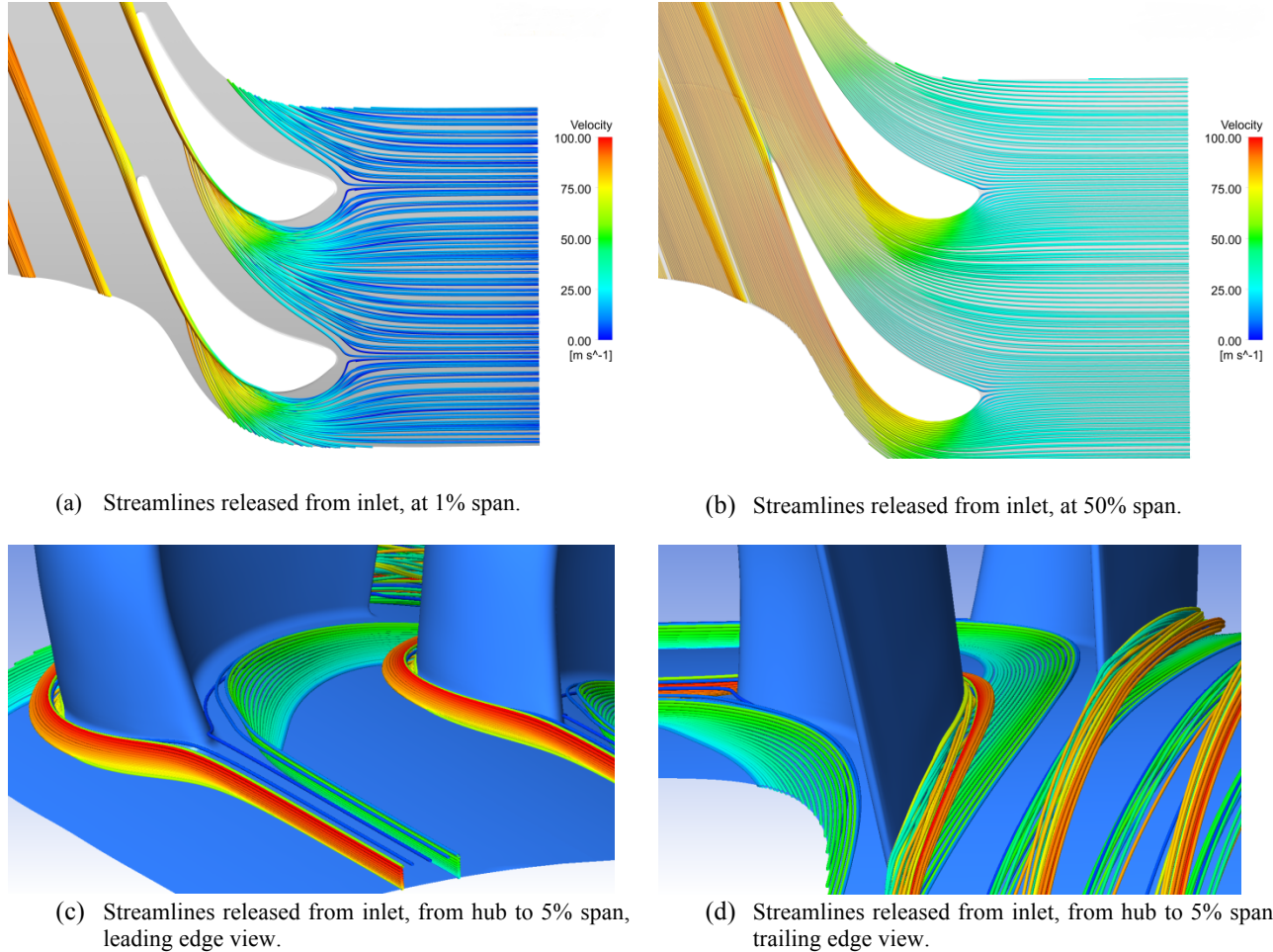


Figure 15. Flow visualization in AFTRF NGV passage.

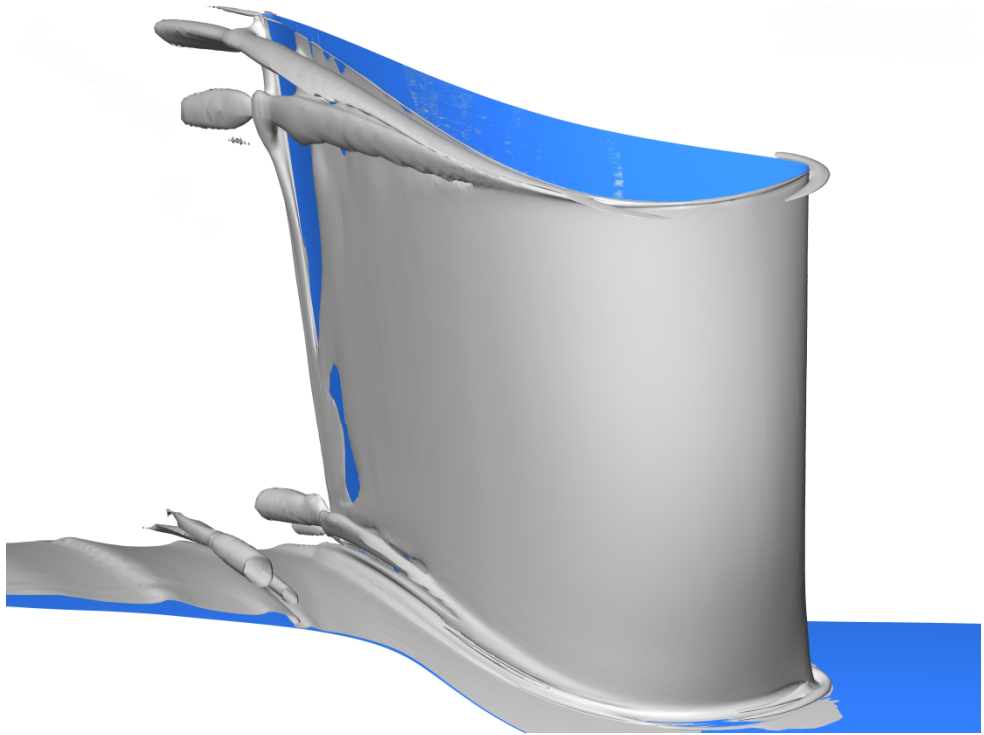


Figure 16. Vortex cores visualized by the Q-criterion.

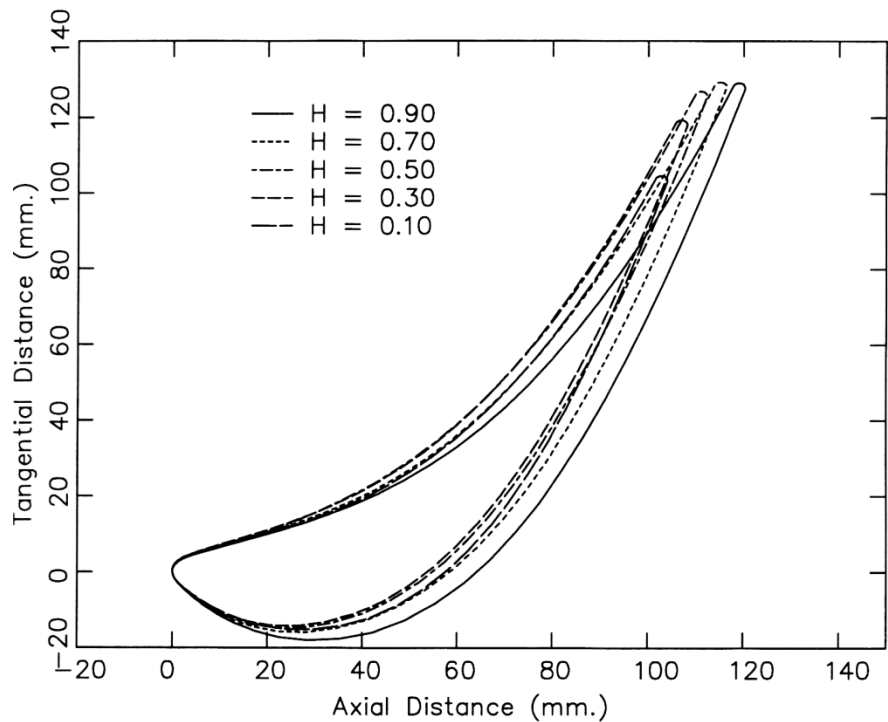


Figure 17. NGV five section profile.

